PHILOSOPHICAL
TRANSACTIONS A

royalsocietypublishing.org/journal/rsta

Research

Cite this article: Panwar V, Vargas CN, Dutcher CS. 2023 Dispersion and mixing dynamics of complex oil-in-water emulsions in Taylor–Couette flows. *Phil. Trans. R. Soc. A* **381**: 20220128.
https://doi.org/10.1098/rsta.2022.0128

Received: 22 August 2022
Accepted: 23 January 2023

One contribution of 16 to a theme issue 'Taylor–Couette and related flows on the centennial of Taylor's seminal *Philosophical Transactions* paper (part 2)'.

Subject Areas:
fluid mechanics

Keywords:
Taylor–Couette flow, navy standard bilge mix, dispersion coefficient, emulsion stability

Author for correspondence:
Cari S. Dutcher
e-mail: cdutcher@umn.edu

Electronic supplementary material is available online at https://doi.org/10.6084/m9.figshare.c.6430088.v3.

THE ROYAL SOCIETY
PUBLISHING

Dispersion and mixing dynamics of complex oil-in-water emulsions in Taylor–Couette flows

Vishal Panwar[1], Cassandra N. Vargas[2] and
Cari S. Dutcher[1,2]

[1]Department of Mechanical Engineering, University of Minnesota – Twin Cities, 111 Church Street Southeast, Minneapolis, MN 55455, USA
[2]Department of Chemical Engineering and Materials Science, University of Minnesota – Twin Cities, 421 Washington Avenue Southeast, Minneapolis, MN 55455, USA

VP, 0000-0003-4495-7659; CSD, 0000-0003-4325-9197

The seminal study by G. I. Taylor (1923) has inspired generations of work in exploring and characterizing Taylor–Couette (TC) flow instabilities and laid the foundation for research of complex fluid systems requiring a controlled hydrodynamic environment. Here, TC flow with radial fluid injection is used to study the mixing dynamics of complex oil-in-water emulsions. Concentrated emulsion simulating oily bilgewater is radially injected into the annulus between rotating inner and outer cylinders, and the emulsion is allowed to disperse through the flow field. The resultant mixing dynamics are investigated, and effective intermixing coefficients are calculated through measured changes in the intensity of light reflected by the emulsion droplets in fresh and salty water. The impacts of the flow field and mixing conditions on the emulsion stability are tracked via changes in droplet size distribution (DSD), and the use of emulsified droplets as tracer particles is discussed in terms of changes in the dispersive Péclet, Capillary and Weber numbers. For oily wastewater systems, the formation of larger droplets is known to yield better separation during a water treatment process, and the final DSD observed here is found to be tunable based on salt concentration, observation time and mixing flow state in the TC cell.

This article is part of the theme issue 'Taylor–Couette and related flows on the centennial of Taylor's seminal *Philosophical Transactions* paper (part 2)'.

1. Introduction

The range of flow states accessible in the flow between two rotating concentric cylinders, or Taylor–Couette (TC) flow, can be used to explore the effects of hydrodynamics on complex fluids and processes. In G. I. Taylor's seminal work in 1923 [1], Taylor aimed to establish a mathematical representation of flow instability between two infinite parallel planes and perform a detailed comparison between results from analysis and experiments. Since it is impossible to carry out experiments with an infinite plane, a set-up with flow between two concentric cylinders was used. Taylor mathematically determined the stability criterion of a given specified initial disturbance and determined that Rayleigh's criterion for stability for inviscid flow is a limiting case of the criterion for a viscous fluid. Taylor also measured the speed for the first appearance of an instability, where he observed that after the symmetrical vortex system, a wavy vortex flow could be accessed. This seminal study by G. I. Taylor (1923) has inspired decades of work in TC flows by providing a dynamic platform to study the flow instabilities. Following Taylor's work, several additional flow states were identified by others [2–9]. Flow states such as Taylor vortices, wavy vortices, modulated wavy vortices, laminar spirals, interpenetrating spirals and some turbulent vortices were mapped as a function of the inner and outer cylinder Reynolds numbers for Newtonian fluids. The versatility of TC platform was also extended beyond Newtonian fluids into non-Newtonian fluid dynamics with exploration in effects of material properties like shear thinning [10,11], viscoelastic nature [12,13] and rheological properties [14] of the fluids on TC flows. Newer flow states like rotating standing waves, disordered oscillations, oscillatory strips, diwhirls, helical vortices, jellyfish-like vortices and viscoelastic turbulence have been observed for non-Newtonian solutions further expanding the usefulness of TC flows [15,16].

The wide variety of precisely controlled and well-studied flow states accessible by the TC cell made it an ideal platform to study complex fluid processes, such as those observed in polymer drag reduction, catalysis, filtration and water treatment [17–30]. For example, efficient and safe heparin anticoagulation has been a problem for continuous renal replacement therapies [18], and Ameer *et al*. tested a device based on TC flow to study simultaneous separation and reaction of heparin removal. TC flows have been used as a rotating wall vessel, which is a suspension culture vessel optimized to produce laminar Couette flow and minimize mechanical stresses on cell aggregates in cell cultures [23–25]. Another example comes from the use of the uniform fluidic motion and mass transport in TC flows for uniform polymer coating on carbon black to control its density and surface charge to achieve black images in electrophoretic displays [26]. Kong & Dennis [27] also demonstrated that a continuous flow Taylor vortex algal photobioreactor can be used to produce and sustain high biomass production and carbon dioxide capture rates. Krintiras *et al*. [28] demonstrated that simple shear flow and heat in the Couette cell can induce fibrous structural patterns to granular mixture of plant proteins for the production of soya-based meat replacements. The TC cell has also been used for improving the efficiency of heterogeneous photocatalysis by nearly a factor of three [29] and commercialized for animal cell cultures in suspension due to the hydrodynamics and mass transfer characteristics it offered [30]. The authors of the current study previously used TC flows and mixing to study hydrodynamic flow field, solution ionic strength and polyelectrolyte molecular weight effects on floc size, growth rate and floc microstructure during the flocculation process [19,31].

The common factor relating these studies is the precise control of the hydrodynamics in the TC cell, and exploration of mixing and axial dispersion dynamics within these flows is of the utmost importance. Recently, the determination of mass transport in the TC cell has been a subject of interest of many studies [26,27,32–40]. For example, Nemri *et al*. [33] have explored the mixing properties of TC flows and the effects of these properties on axial dispersion of a passive tracer using both experiments and numerical simulations. Mass transport has been studied in terms of advective transport from vortex structures with two different mechanisms: inter- and intra-vortex transport. Whether it be experimentally through residence time distribution [33–35], laser-induced fluorescence [33,36] or modelling the vortex as a two zone [37] or well-mixed reactors [35], several of the prior studies that explored mixing and mass transport have done so for one or two flow states. In addition, there have been mechanical restrictions from the TC geometry for single injection locations either through the top of the annulus or through holes in the outer cylinder. These restrictions might affect the precise control over the flow as the presence of capillary in annulus can alter the local flow profile. Wilkinson & Dutcher [41,42] designed a new and modified TC cell that incorporates 16 injection ports uniformly distributed axially and azimuthally into the inner cylinder. The non-intrusive nature of the design allows injection of large fluid volume into the annulus during the co- and counter-rotation operations of the TC cell.

In this study, the TC cell designed by Wilkinson & Dutcher [42] is used to explore the formation and dispersion of model oily shipboard wastewaters in a variety of different TC flow conditions. Oil leaks from machinery and maintenance activities mixes and combines with water collected in the bilge, which is the lowest chamber, of a naval ship, resulting in the formation of complex wastewater emulsions. Various types of fuels, lubrication oils, cooling water, detergents and solvents are contained in these emulsions. Bilgewater pollution accounts for around 20% of millions of tons of oily wastewater discharged into the ocean [43–45]. Hence, oily emulsion is regulated by MARPOL Annex 1 and for Armed Forces vessels, DoD Regulation (U.S. DoD 2017), where the discharge oil content must be below 15 ppm [46,47].

A key challenge for on board oil abatement systems is the presence of small droplets, where oil droplets less than 20 µm in diameter are particularly difficult to separate [48]. One key tool that can be further optimized to help with the oil treatment is the hydrodynamic flow field the emulsion experiences during treatment. The distribution of droplet sizes in an emulsion during treatment is influenced by the mixing intensity or the flow conditions [48], as mixing and shear effects can impact droplet dispersion and droplet-droplet interactions. Farzad *et al.* [49] investigated the droplet size distribution (DSD) of liquid–liquid emulsions in TC flows, where dispersion effects dominate over diffusion, influencing the number of collision events between droplets. In addition, shear-induced coalescence of stabilized emulsion droplets under simple shear flow or Couette flow has been explored in various studies [50–55]. In general, the surfactant concentration or surface charge distribution can become heterogeneous under shear, leading to destabilization and coalescence when two droplets come into contact [55,56]. Our recent concurrent work has focused on the stability of pre-prepared oil-in-water emulsions under a variety of shear rates available in TC flows and complexity of dispersion and DSD in TC flows.

In the current work, we explore the intermixing rates, mixing dynamics and emulsion DSD of chemically complex oil-in-water emulsions injected into well-controlled flow states established within the TC cell. The dispersion is quantified via the determination of apparent intermixing coefficients in both distilled water and in a saltier environment. The DSD of the emulsion is also determined at various stages of mixing to identify the effects of mixing speed and observation time scale on the stability of the emulsion formation.

2. Materials and methods

(a) Materials

The emulsion systems used here are complex oil-in-water emulsions, made with specifications provided by the Strategic Environmental Research and Development Program (SERDP) and Naval Surface Warfare Center Carderock Division (NSWCCD). A Navy Standard Bilge Mix (NSBM#4) consisting of 50% (vol/vol) Marine diesel fuel (MIL-PRF-16884), 25% (vol/vol) TEP Steam Lube Oil 2190 (MIL-PRF-17331) and 25% (vol/vol) Diesel Lube Oil 9250 (MIL-PRF-9000) was specified as the dispersed oil phase for this system and will be referred to as NSBM#4 from here on in this study. The NSBM#4 oil has a density of 853 kg m^{-3}, kinematic viscosity of 31.2×10^{-6} m^2 s^{-1} and interfacial tension of 17.2 mNm^{-1} at 20°C [57]. A detergent blend of 50% (vol/vol) Type-1 General Purpose Detergent (MIL-D-16791G(1)), 25% (vol/vol) commercial liquid Tide Ultra® detergent, and 25% (vol/vol) degreasing solvent (MIL-PRF-680C, Type III) was specified as the surfactant mixture pre-loaded into the continuous water phase and will be referred to as SERDP surfactant mix from here on.

All concentrated emulsion samples used in this study were blended with a rotor-stator homogenizer (IKA: T-25 digital Ultra-Turrax) for a fixed duration (120 s) and at a fixed homogenization rate (20 000 r.p.m.). A 4% (vol/vol) NSBM#4 with 100 ppm SERDP surfactant mix was prepared using the homogenizer for a total volume of 50 ml. This concentrated emulsion was used for injection into the annulus and prepared immediately before performing each experiment. The annulus of the TC cell was loaded with 100 ppm SERDP surfactant mix in distilled water (Premium Water, Inc.). This was mixed before loading into the TC cell using a Jiffy mixer attachment for 30 min in 1 L glass jars. The concentrated (4% NSBM#4) emulsion and emulsion-free surfactant water solution were prepared in such a way to obtain a final concentration of 0.1% NSBM#4 and 100 ppm SERDP surfactant in the solution after injection into the annulus of the cell. For the salinity studies, the solutions were prepared in the same way, with the addition of NaCl to yield a final NaCl concentration of 10 mM. It is anticipated based on work with a similar oil and surfactant mix system [58], though with synthetic seawater aqueous phase, that the interfacial tension values at this concentration would drop to near 8 mN m^{-1}. The kinematic viscosity of the final 0.1% (v/v) NSBM#4 mix solution at 22°C was measured to be 9.803×10^{-7} m^2 s^{-1} and the density 0.997 g ml^{-1}. While the system studied here is informed by a specific application of shipboard water treatment, certainly the insights of hydrodynamics on emulsion stability can be generally extended to chemically stabilized oil-in-water emulsions in a variety of applications.

(b) Taylor–Couette geometry and flow visualization

The TC cell used in this study is a custom TC cell design that houses 16 injection ports evenly spaced axially and azimuthally along the inner cylinder. These injection ports do not protrude into the annulus, and the port covers are contour-matched to the inner cylinder so that the flow profile of the resultant vortices is not modified during operation. The design has been described in previous work [41]. In brief, the inner cylinder is made of anodized aluminium and the outer cylinder is made of borosilicate glass. The inner diameter is 13.54 cm, the annulus height is 51 cm and radial gap width is 0.84 cm, resulting in a radius ratio of 0.89 and height-to-gap (aspect) ratio of 60. The top and bottom of the annulus are fixed to the outer cylinder and kept stationary in the current work. Each injection port is connected to a check valve with 10 psi crack pressure and a flow restrictor to normalize flow between injection ports.

A laser diode (Thorlabs, 450 nm, 1600 mW max) in combination with a laser line generator was used to create a laser light sheet tangential to the inner cylinder. A Basler Ace camera (1280 × 1024 pixels, 60 fps maximum frame rate) with a Tamron 25 mm c-mount lens was vertically adjusted such that the field of view was between the third and fourth injection port row covers from the top of the TC cell. The frame rate on the camera was set to 60 fps with an exposure time of 8 ms for all experiments. The solution containing 100 ppm SERDP surfactant mix and distilled water (or 10 mM NaCl in salt cases) was transferred into the TC cell using a tube connected to the base of the cylinder assembly. A figure detailing this process can be found in previous studies by Metaxas *et al.* [19,31].

(c) Injection flow calibrations

As mentioned in Wilkinson & Dutcher [42], the mass injection through the inner cylinder was first calibrated. To perform the calibration, the inner cylinder and port covers were removed from the assembly. Scintillation vials were attached to the end of each injection ports and fluid sample masses were measured at a variety of injection times at 30 psi pressure. Figure 1 shows

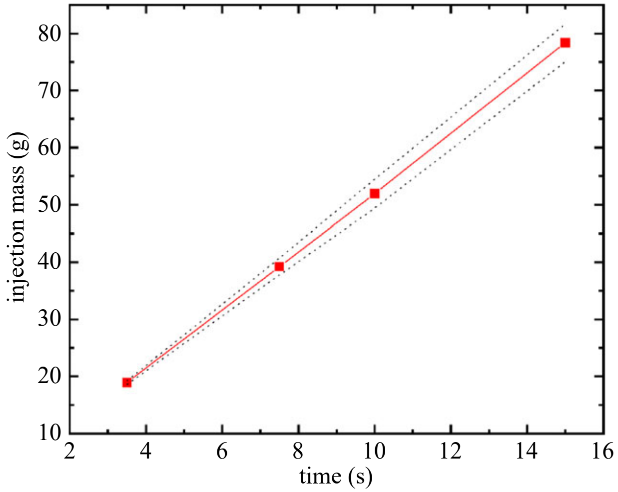

Figure 1. Injection mass flow rate calibration with 30 psi injection pressure for 4% (v/v) NSBM#4 concentrated emulsion. The solid lines represent the best-fit linear regression used to quantify the mass flow rates. The dashed lines are the 95% confidence intervals for the linear regression. (Online version in colour.)

the mass flow rate calibrations with 95% confidence intervals. All experiments were performed at a 30 psi injection pressure at a calibrated injection rate of 5.23 g s^{-1} for both no salt and 10 mM NaCl cases.

(d) Mass transfer experiments

The TC cell can generate a wide variety of flow states as a function of cylinder speed and fluid properties. TC flow dynamics are characterized by the Reynolds number (*Re*) for both inner and outer cylinders, defined as

$$Re_{\text{in, out}} = \frac{\Omega_{\text{in, out}} R_{\text{in, out}} d}{\nu}, \tag{2.1}$$

where Ω refers to the angular velocity, R is the cylinder radius, d is the width of the annulus, or gap, between the two cylinders ($d = R_{\text{out}}$ - R_{in}), and ν is the kinematic viscosity of the fluid enclosed within the annulus. Five different *Re* values, over three different flow states, were used in this study, including (i) laminar wavy vortex flow (LWV), (ii) turbulent wavy vortex flow (TWV) and (iii) turbulent Taylor vortex flow (TTV). The 'turbulent' cases of the wavy vortex and Taylor vortex physically resemble their laminar counterparts, with additional turbulent features such as eddies [9]. The desired flow states were established using a constant rotation speed prior to emulsion injection: 0.20 s^{-1} (LWV), 0.56 s^{-1} and 0.74 s^{-1} (TWV) and 1.11 s^{-1} and 1.48 s^{-1} (TTV). These cylinder rotation speeds were selected so the corresponding *Re* number falls in the range of relevant flow states [9,41].

The pixel brightness of the concentrated oil emulsion was used as a way to visualize the transfer between vortices and ultimately calculate vortex mass transfer. The field of view was restricted between two rows of ports to increase spatial resolution. A LabView code was used to control the injection of the concentrated emulsion from the inner cylinder ports into the annulus as well as to record visualizations of the entire mass transfer process. To start the experiment, the inner cylinder drive shaft and injection ports were primed with the emulsion. The flow state was established at a fixed cylinder rotation speed, maintaining the rotation rate for 10 min for the flow states vortices to stabilize before the start of the experiment and recording was then started. After an initial delay of 30 s, 50 ml of concentrated 4% (v/v) NSBM#4 emulsion was injected through the inner cylinder into the annulus at an injection rate of 5.23 g s^{-1}. This was maintained for 30 min to allow the emulsion to disperse into the cell, and 20 ml samples were collected every 10 min from the start to measure the corresponding DSD using a laser diffraction size analyser.

After completion of each experiment, the TC cell was disassembled and cleaned. All speeds were repeated three times for statistical accuracy for both salt and no salt cases, resulting in a total of 30 complete assembly steps. Since in the wavy states of LWV and TWV, the boundary moves axially, the midpoint of each azimuthal wave was identified visually, and the average axial location was used. Time-dependent spatial variations in concentration after injection were used to determine the mass transport coefficients, which are described below. Fourier analysis on the time and spatial variations was also used to confirm the vortex structure type in the flow and the detailed process is described in Dutcher *et al.* [9,41].

(e) Image analysis

As mentioned in Wilkinson & Dutcher [42], the concentration of emulsion was measured by quantifying the intensity of light reflected by the emulsion droplets in the solution. The pixel intensity of each vortex is averaged, producing a single concentration per vortex, based on a linear intensity-concentration scaling. The intensity to concentration calibration per vortex can be described with the following equation:

$$C = \frac{I - I_o}{I_f - I_o} \times \frac{m}{V_o + (m/\rho)}, \tag{2.2}$$

where C is the concentration of the emulsion (g L^{-1}), I is the instantaneous average pixel intensity, I_o is the zero concentration (pre-injection) intensity, I_f is the final concentration intensity, m is the mass of the emulsion injected in grams and ρ is the density of the concentrated solution, which was measured to be 997.6 ± 1.1 kg m^{-3}. V_o is the initial volume of distilled water in the annulus and end cap area, which is equal to 1.95 L. Further details can be found in previous work [42].

Once the time profile of emulsion concentration for each vortex was obtained, an intermixing coefficient can be determined by regression. Analysis methods similar to [42] were used, which are based on equation (2.3) by Ohmura *et al.* [34]. Similar to [42], each vortex is treated as an individual well-mixed vortex reactor. The mass transfer across the interfacial area between the adjacent vortices was averaged for each vortex to obtain a single concentration per vortex per frame. The mass balance for the nth vortex can be calculated using the following equation.

$$V_n \frac{dC_n}{dt} = kS(C_{n+1} - 2C_n + C_{n-1}), \tag{2.3}$$

where C_n is the concentration of the nth vortex (the vortex of interest) and subscripts $n+1$ and $n-1$ correspond to adjacent vortices. V_n is the volume of the nth vortex $[\pi\,(r_o{}^2 - r_i{}^2)L_n]$, S is the interfacial area between vortices $[\pi\,(r_o{}^2 - r_i{}^2)]$ and k is the intermixing coefficient.

To determine the best-fit k for each experiment, the *fsolve* function in MATLAB was used to minimize the mean square error between the predicted vortex concentrations over time and the measured values. The experimentally measured concentrations in the vortices located just above the fourth-row injection port and the vortex located just below the third-row injection port were used as boundary conditions in the determination of k. The intermixing coefficient can then be linearly converted to an effective dispersion coefficient as $D_z{}^* = 2\lambda k$ [34,42], where λ is the axial wavelength and $D_z{}^*$ is the effective dispersion coefficient. For consistency with our prior study [42], the vortex height is used here as the axial wavelength, which is of order of approximately 1 cm.

(f) Droplet characterization: laser diffraction particle size analyser

To determine the influence of dispersion and shearing on the emulsion stability, measurements of the emulsified DSDs of samples taken both before, during and after experimentation were performed. Laser diffraction particle size analysis was conducted using a Bluewave Laser

Diffraction Particle Size Analyzer (Mictrotrac®). The method is based on the scattering of a laser beam from the emulsified droplet, where the angles of diffraction are correlated to the particle size. Number-based size distributions, volume-based size distributions and oil volume concentration of different diameter peaks and mean volume diameter were collected in all cases.

3. Results and discussion

(a) Mass transfer analysis

Mass transfer experiments were conducted at five *Re* values: a single *Re* value for LWV ($Re = 700$) and two different *Re* values for TWV ($Re = 2040$ and 2700) and TTV ($Re = 4050$ and 5400) and corresponding intermixing coefficients (k) were determined from equation (2.3). For each of the nominally turbulent flow states, *Re* values were selected such as one was near the lower end and the other near the higher end of *Re* range for that flow state, so that both the effect of changing *Re* as well as changing flow state can be explored. A concentrated (4% v/v) NSBM#4 oil emulsion was injected at a specified *Re* value for the corresponding vortex structure using the 16 injection ports that are uniformly located along the inner cylinder. The modelling of the mass transport of the injected liquid in stable TC flow fields has been discussed previously in an earlier publication [42], where each vortex was treated as a well-mixed reactor and the intermixing and dispersion coefficients were determined. The timescale used for non-dimensionalization is the viscous timescale based on the gap, $\tau_\nu = d^2/\nu$, matching that used previously [42] and corresponding to the timescale for vortex decay for higher aspect ratio systems [59], similar to that which was used here ($\Gamma = H/d = 60$, with H, height and d, gap). However, it should be noted that this is only one example of the Rayleigh viscous timescale of $\tau = L^2/\nu$ for TC flows, where L is the characteristic length. Other viscous timescales include those based on length of the cell, H^2/ν [60–62], a combination of length and gap, Hd/ν [61,63–65] or the timescale for spin-up of fluid between a pair of rotating discs, $H/(\nu\Omega)^{1/2}$ [60,66], where Hd/ν is found to more correctly account for the steady state for the onset of vortices in the flow [59].

An example of emulsion injection and dispersion is shown in figure 2 for the lowest flow state tested, LWV, $Re = 700$. The axial location of annulus between two injection port rows was captured after injection and the intensity was regressed to find the intermixing coefficients, according to equations (2.2) and (2.3). The corresponding concentration profiles (figure 2*b*) shows the respective changes in the concentration of different vortices with time and collapse to a final value. The rate of collapse to the final equilibrium concentration depends on the intermixing rate which was used to qualitatively compare the dispersion between different flow states and *Re*. The apparent intermixing coefficient (k) for the LWV was found to be ($1.37 \times 10^{-1} \pm 9.21 \times 10^{-3}$) cm s^{-1} and was calculated from the average of three runs per flow state. The intermixing coefficient can be linearly converted to the effective dispersion coefficient, resulting in a value of ($2.75 \times 10^{-1} \pm 1.84 \times 10^{-2}$ cm^2 s^{-1}) for LWV flow. Figure 2*b* highlights the changes in the vortex concentration based on the brightness of the vortices, vortices 1 and 9 start with high concentration as the injection takes place in these vortices but gradually the concentrated emulsion was dispersed between the vortices present between the injection port rows.

The next flow state tested was the TWV, at two different *Re* values (2040 and 2700). Figure 3 shows that the emulsion disperses faster here compared with LWV. Using the same method as above, the intermixing coefficient, k increased to ($2.35 \times 10^{-1} \pm 2.87 \times 10^{-2}$) cm s^{-1} for $Re = 2040$ and ($2.50 \times 10^{-1} \pm 2.06 \times 10^{-2}$) cm s^{-1} for $Re = 2700$. Interestingly, the increase in *Re* resulted in only a slight increase in the intermixing coefficient within the TWV flow state. By contrast, the intermixing coefficient for TWV was approximately doubled compared with LWV. In addition to the turbulent nature of TWV, other complex droplet-flow effects discussed in later sections might be responsible for the difference. As before, the intermixing coefficient can be converted to dispersion coefficient, $D_z{}^*$, for TWV and was found to be ($4.70 \times 10^{-1} \pm 4.28 \times 10^{-2}$) cm^2 s^{-1} for

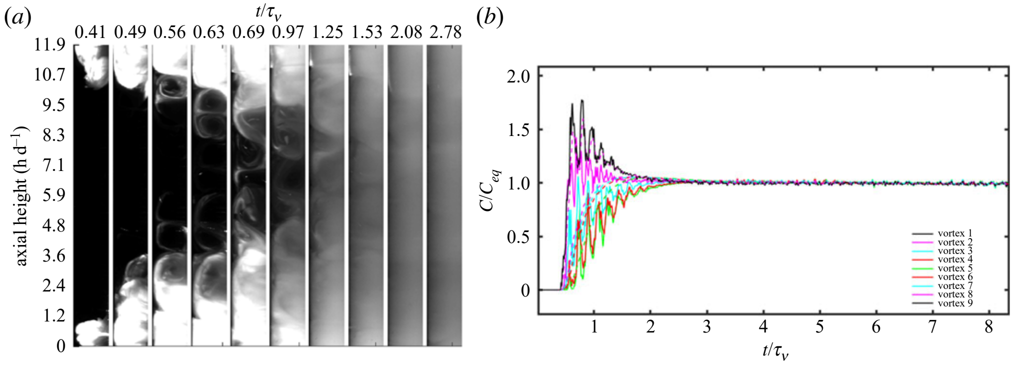

Figure 2. Mass transfer results for LWV structure ($Re = 700$) at 30 psi, 50 ml injection. (*a*) Snapshots (0.84 cm wide) of portions of the annulus between two injection port rows after injection of the concentrated emulsion, illustrating the spatial concentration in the projected θ-z plane evolving in dimensionless time, t/τ_ν, of each image. (*b*) Temporal profile of the concentration, based on equation (2.2), in several vortices (solid lines) and the model (dashed lines) using the best-fit intermixing coefficient from equation (2.3). The y-axis is normalized by the final equilibrium concentration of emulsion, and the x-axis is dimensionless time, time divided by the viscous timescale ($\tau_\nu = 71.97$ s). The black (vortex 1) and grey (vortex 9) lines correspond to the outermost vortices that are used as the input boundary conditions in the model regression. (Online version in colour.)

$Re = 2040$ and $(5.00 \times 10^{-1} \pm 4.13 \times 10^{-2})$ cm^2 s^{-1} for $Re = 2700$. The value of dispersion coefficient within the flow state does not significantly increase, even with an increase in *Re*.

The last flow state, TTV, was tested at two different *Re* values (4050 and 5400). At this highest flow state, shown in figure 4, the emulsion spreads at a significantly faster rate in the annulus of the TC cell compared with the lower order flow states. The intermixing coefficients, *k*, were found to be $(6.05 \times 10^{-1} \pm 3.64 \times 10^{-2})$ cm s^{-1} for $Re = 4050$ and $(7.12 \times 10^{-1} \pm 3.75 \times 10^{-2})$ cm s^{-1} for $Re = 5400$. The intermixing coefficient was found to be significantly higher than the values found for TWV and LWV, approximately three times the value of TWV and five times the value of LWV. In addition, the intermixing coefficient observed an increase of approximately 20% over the *Re* range from 4000 to 5400. Likewise, the $D_z{}^*$ for TTV was found to be $(1.21 \pm 7.28 \times 10^{-2})$ cm^2 s^{-1} for $Re = 4050$ and $(1.42 \pm 7.50 \times 10^{-2})$ cm^2 s^{-1} for $Re = 5400$. The dependence of apparent intermixing coefficient normalized by injection velocity on *Re* is shown in figure 5 (filled symbols for the 0 mM 'no salt' systems).

In the salt case, 10 mM NaCl was added to the emulsion system to determine the effects of salinity on the emulsion dispersion and stability since these oily wastewater emulsions are usually formed in a saline environment. Experimental protocol similar to the 'no salt' case was followed, where the desired flow states were established at the specified *Re* values. The full set of mass transfer results, including the visualization and the temporal concentration profiles, for all cases with the aqueous salt solutions are provided in the electronic supplementary material, figures S1–S3. The resultant intermixing coefficients are also shown in figure 5 (open symbols, for the 10 mM systems). For LWV, the intermixing coefficient, *k*, was found to be $(2.61 \times 10^{-1} \pm 7.67 \times 10^{-2})$ cm s^{-1}, approximately twice the value of the no salt case, indicating a faster spread of emulsion in the presence of salt. The TWV flow state observed a similar increase in *k* values, where *k* was found to be $(3.22 \times 10^{-1} \pm 6.70 \times 10^{-2})$ cm s^{-1} for $Re = 2040$ and $(3.66 \times 10^{-1} \pm 6.47 \times 10^{-2})$ cm s^{-1} for $Re = 2700$. Lastly for the TTV flow state, the intermixing coefficients, *k*, were measured and reported as $(6.70 \times 10^{-1} \pm 3.44 \times 10^{-2})$ cm s^{-1} for $Re = 4050$ and $(8.35 \times 10^{-1} \pm 8.47 \times 10^{-2})$ cm s^{-1} for $Re = 5400$. The dispersion coefficient values were found to be higher for all salt cases compared with no salt cases, possibly due to changes in the DSD and droplet stability, reported and discussed in the next sections, but the percentage of increase reduces with increasing *Re*. Overall, it is clear that as *Re* increases, inter-vortex mass transfer

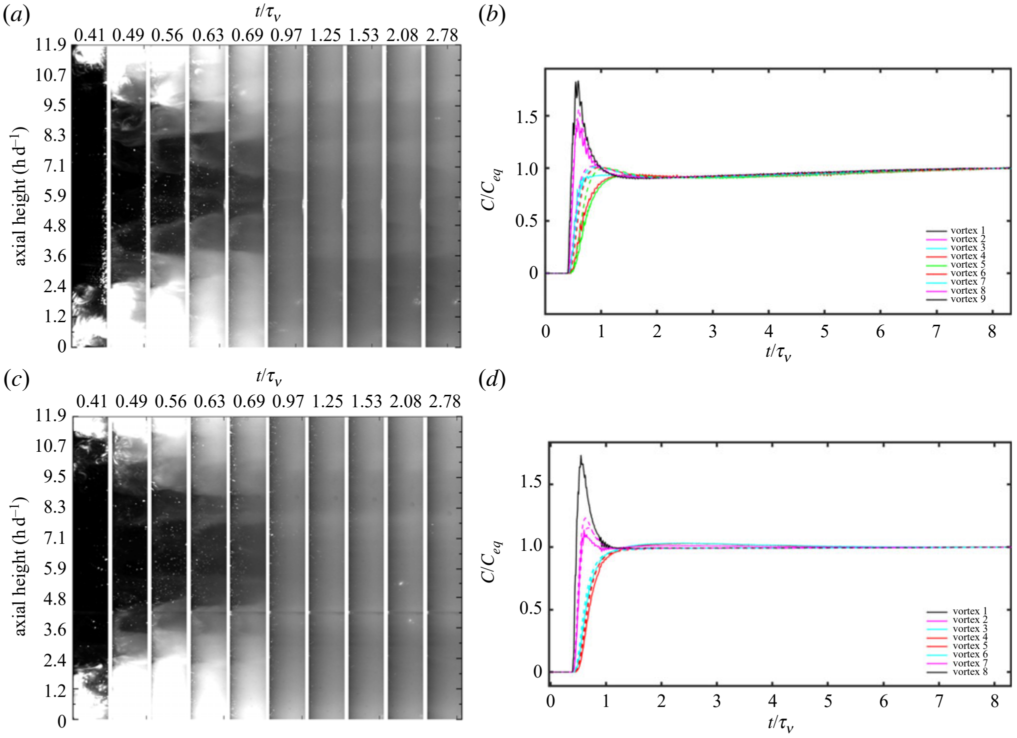

Figure 3. Mass transfer results for TWV structure at 30 psi, 50 ml injection for (*a,b*) $Re = 2040$ and (*c,d*) $Re = 2700$. (*a,c*) Snapshots of the annulus between two injection port rows after injection of the concentrated emulsion, illustrating the spatial concentration in the projected θ-z plane evolving in dimensionless time, t/τ_v, of each image. (*b,d*) Temporal profile of the concentration in several vortices (solid lines) and the model (dashed lines) using the best-fit intermixing coefficient. (Online version in colour.)

as measured by changes in light intensity with the mixing of emulsified droplets also increases (figure 5), as expected [33,42]. Slight deviations in the trend may be due to additional dynamics of the emulsified droplets, as these droplets can coalescence, aggregate and deform under shear. The changes in the DSD of emulsion are explored in the next section, with comparison of key dimensionless groups for the emulsified droplets compared with solid flakes, in the section to follow.

(b) Droplet size distribution in mixing Taylor–Couette flows

The correlation between the intermixing and DSD of oil-in-water emulsions in the TC flows was examined at two different stages of mixing during the experiments, to determine the effects of timescale of observation as emulsions are inherently unstable and destabilize over time. As explained in the Methods section, samples were collected at the 10 min mark for the initial mixing stage and at the 30 min mark for the final mixing stage; time was normalized in plots by the viscous timescale ($\tau_v = 71.97$ s). Furthermore, the results discussed here are in the terms of the volume size distribution plots along with volume mean diameter, D_{mv}, and the per cent of oil volume distribution in the largest diameter peak (third diameter peak), D_{p3} of the volume DSD, as the larger droplets have the most effect on destabilizing and creaming of the emulsion. Initially, in the emulsion prepared for injection, the concentrated emulsion (4% v/v NSBM#4) showed a $D_{mv} = 11.72\,\mu$m and no third diameter peak, D_{p3}.

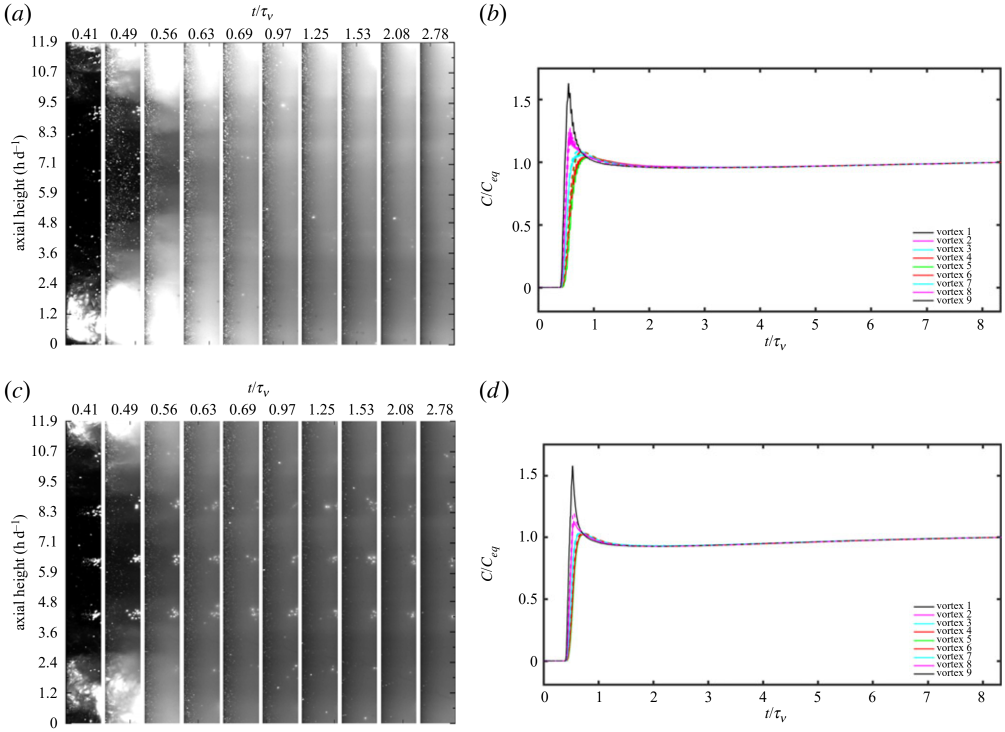

Figure 4. Mass transfer results for TTV structure at 30 psi, 50 ml injection for (*a*,*b*) $Re = 4050$ and (*c*,*d*) $Re = 5400$. (*a*,*c*) Snapshots of the annulus between two injection port rows after injection of the concentrated emulsion, illustrating the spatial concentration in the projected θ-z plane evolving in dimensionless time, t/τ_ν, of each image. (*b*,*d*) Temporal profile of the concentration in several vortices (solid lines) and the model (dashed lines) using the best-fit intermixing coefficient. (Online version in colour.)

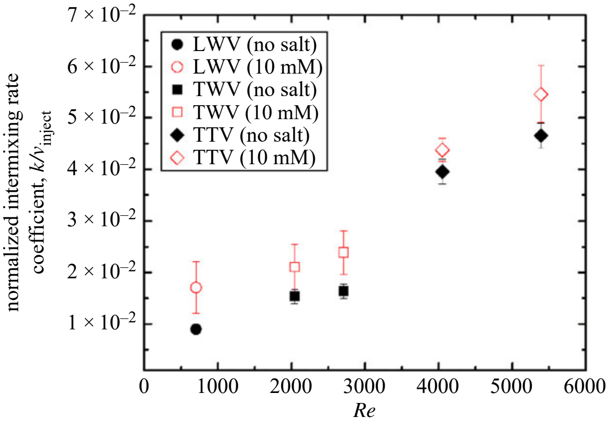

Figure 5. Normalized intermixing rate coefficient (k/v_{inject}) with increasing *Re* for all vortex flow states with 50 ml injection in no salt (filled symbol) and 10 mM NaCl (open symbol) at 30 psi in TC cell. The intermixing coefficient is non-dimensionalized using the injection velocity ($v_{\text{inject}} = 15.3\ \text{cm s}^{-1}$) and was found to be increasing with *Re*. (Online version in colour.)

For the initial mixing stage, the effects of intermixing on the DSD of the emulsion are most apparent. A lower dispersion rate means that the concentrated emulsion does not disperse uniformly in the annulus between the vortices, but rather remains longer in a single vortex nearest

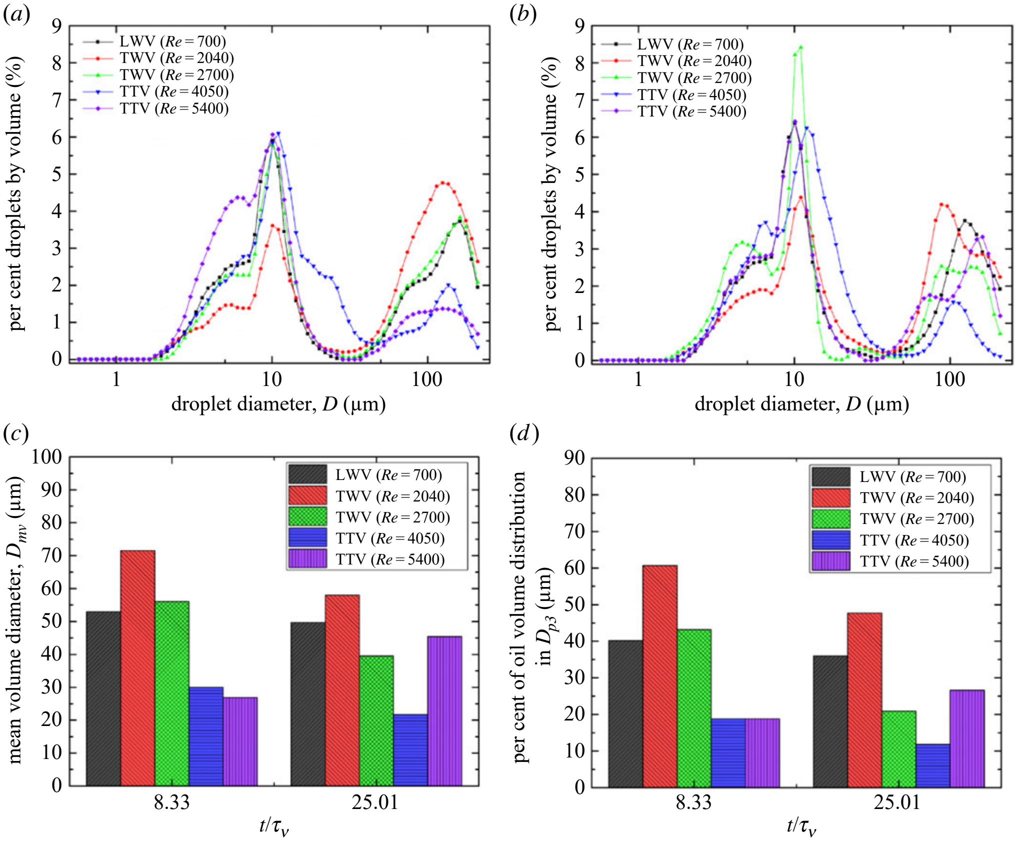

Figure 6. (*a*,*b*) DSD by volume per cent at (*a*) initial mixing stage $t/\tau = 8.33$ and (*b*) final mixing stage $t/\tau = 25.01$ for *Re* ranging from 700 to 5400. (*c*) Mean volume diameter, D_{mv} and (*d*) per cent of oil volume distribution in the third diameter peak, D_{p3} for TC flow states ranging from LWV, TWV and TTV with a final concentration of 0.1% NSBM#4 oil mix, 100 ppm SERDP surfactant mix in distilled water at initial and final stages of mixing after injection. (Online version in colour.)

to the injection port. The longer it remains in a vortex (the smaller the dispersion rate), the higher chances of collisions and coalescence events within that concentrated vortex. As the emulsion disperses, it becomes diluted, and the chances of collisions and coalescence between the emulsion droplet are reduced. In our previous work, we have found that DSD varies non-monotonically with shear rate, indicating an existence of optimal shear rate at which the droplet coalescence is maximum. Exceeding this critical shear rate results in reduced bridging time and increased collision frequency in the higher shear rate mixing environment leading to droplet breakup. From the measurements of DSD for the initial mixing stage, as shown in figure 6*a* at $t/\tau_v = 8.33$, coalescence increases at an optimal shear rate of TWV, where the volume mean diameter, D_{mv}, was found to be highest (approx. 71.5 μm) for TWV at $Re = 2040$ and reduces on further *Re* increase. The lowest D_{mv} values were found for highest *Re* flow states, corresponding to a combined effect of the droplet breakup at higher mixing rates. This shows that higher intermixing rates spread the emulsion droplets more effectively and uniformly between vortices, reducing the time available for intra-vortex mixing and coalescence, hence the D_{mv} values were reduced at higher dispersion rates. It should be noted that LWV offers the lowest intermixing rate, but also has a lower amount of shear rate and internal mixing within the vortex compared with TWV, which relates to the optimal shearing rate for increasing collision frequency while providing enough bridging time for coalescence and aggregation.

For the highest flow state TTV, D_{mv} was found to be around 25–30 μm for both $Re = 4000$ and 5400. However, the reduction in D_{mv} was relatively insignificant within the range of TTV, compared with a large increase in *Re*, indicating there might be limits to which droplet size can be affected by mixing rates. The per cent of oil volume distribution in the third peak diameter, D_{p3}, shown in figure 6*d*, and the peaks that can be seen in figure 6*a* around approximately 100 µm droplet diameter, demonstrate similar results. Higher percentages of oil volume distribution were found for TWV ($D_{p3} = 109$ µm at 60% for $Re = 2040$ and 117 µm at 43% for $Re = 2700$) and LWV ($D_{p3} = 119$ µm at 40%) but volume distribution per cent of $D_{p3} = 112$ µm reduced to 19% for TTV, showing that injection at lower flow order flow states results in more per cent of volume distributed in larger droplet sizes (higher coalescence at lower intermixing rates). By contrast, the higher dispersion rate of TTV disperses the emulsion more effectively and breaks up the droplets due to higher shear rate, this results in formation of more stable emulsions with smaller droplet mean volume diameter.

Even after the dispersion was completed and the emulsion was uniformly distributed in the annulus, the DSD continues to evolve as emulsion are inherently complex and their behaviour depends on surface chemistry, mixing rate as well as timescale of observation. For the final mixing stage, the samples collected at $t/\tau_\nu = 25.01$ (shown in figure 6*b*) were used to analyse these long-term timescale effects in correlation with mixing and shearing on emulsion stability. It can be seen from figure 6*b* that the overall values of the DSD are lower for the final mixing stage compared with the initial stage, mainly due to the emulsion destabilizing over time and larger size droplets separating out of the solution, this is further explained in the next section with the help of settling time. For both LWV at $Re = 700$ and lower end of TWV at $Re = 2040$, the mean volume diameter, D_{mv}, was largest among the final mixing stage at 49 µm and 58 µm, respectively. The per cent volume distribution of D_{p3} also observed similar higher values at $D_{p3} = 120$ µm at 36% for LWV ($Re = 700$) and $D_{p3} = 102$ µm at 48% for TWV ($Re = 2040$). The higher values of D_{mv} correspond to the optimal shear rates present at LWV ($Re = 700$) and TWV ($Re = 2040$), which increases the frequency of droplet collisions and provides enough bridging time for maximum shear-induced coalescence. Moving to higher *Re* of TWV and TTV, as shown in figure 6*c*, the mean volume diameter decreased for TWV ($Re = 2700$) and TTV ($Re = 4050$) but increased slightly for higher *Re* TTV ($Re = 5400$). The higher shear rates present at high *Re* value flow states can result in increased collision frequency leading to increased droplet breakup, lower bridging times and ultimately decreased droplet coalescence. In general, lower *Re* values of LWV and TWV form less stable emulsions, compared with higher *Re* TTV flow states, as the emulsion formed at lower *Re* exhibits higher mean volume diameter and higher per cent of volume distribution in the largest diameter peak at both the initial as well as the final stages of mixing. The TWV state at $Re = 2040$ was found to be the optimal mixing state of those explored for forming the most unstable emulsions with higher mean volume diameter, D_{mv} (approx. 71.5 µm and 58 µm) and highest per cent volume distribution at D_{p3} ($D_{p3} = 109$ µm at 60% and $D_{p3} = 102$ µm at 48% for $Re = 2040$) at both initial and finals stages of mixing, respectively.

In addition to the effects of shearing and mixing timescales, salinity is another key factor for emulsion stability as these types of emulsion are typically formed in a saltwater environment. Historically, it is evident from studies like [57,67,68] that salt decreases the stability of oil-in-water emulsions stabilized by ionic and non-ionic surfactants. Church *et al*. [67] observed that addition of NaCl in the presence of surfactants reduced the interfacial tension to a varying degree, depending on the amount added, resulting in lower interfacial tension, which indicates formation of smaller droplets as the energy requirement is reduced. However, as confirmed by other studies and visual observation, emulsions are less stable in the presence of NaCl. This difference is explained by another work on the topic by Davis *et al*. [69], where lower interfacial tension due to the addition of salt can lead to the formation of smaller droplets that can reduce the number of coalescence events, while other destabilizing mechanisms like flocculation, aggregation and creaming were still observed due to the reduced electrostatic repulsion between the droplets. The combined effects of salt, timescale of observation and mixing at different speeds complicates the understanding of the process. Here, the changes in DSD were determined for the system with 10 mM NaCl like the no salt case, shown in figure 7. Initially, the injected concentrated emulsion (4% v/v NSBM#4 with 10 mM NaCl) was found to have a $D_{mv} = 11.77$ µm and no third peak,

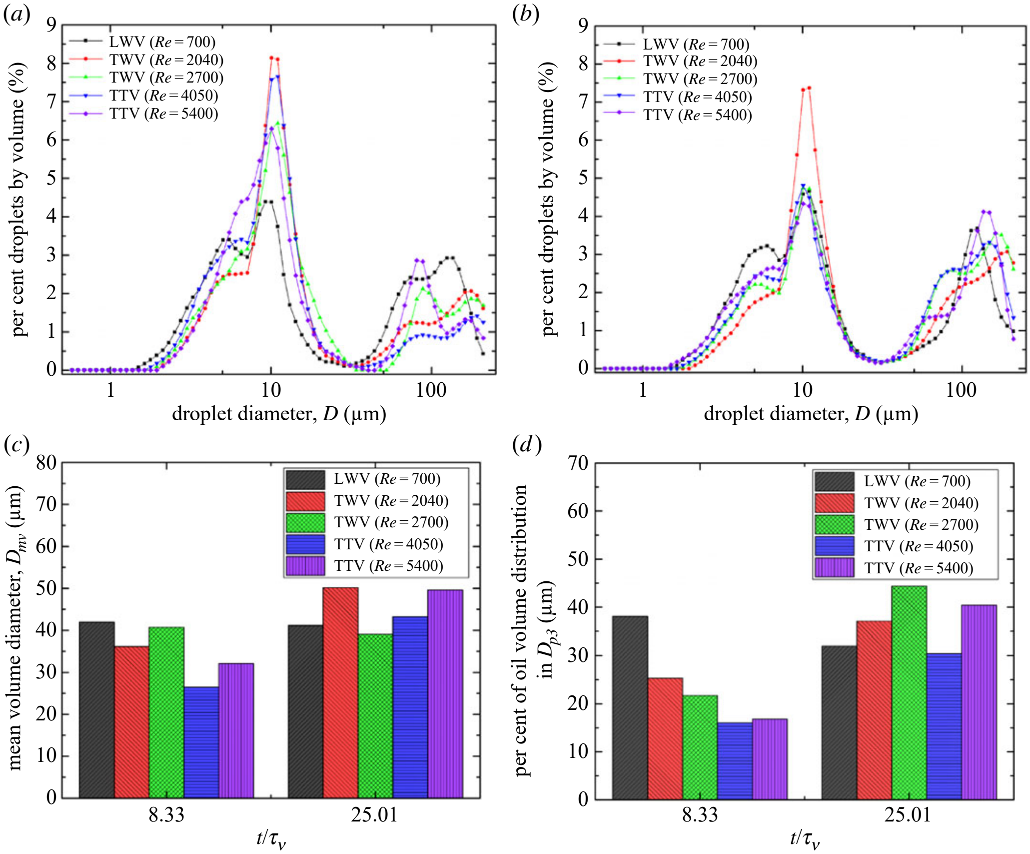

Figure 7. (*a*,*b*) DSD by volume per cent at (*a*) initial mixing stage $t/\tau = 8.33$ and (*b*) final mixing stage $t/\tau = 25.01$ for *Re* ranging from 700 to 5400 with 10 mM NaCl. (*c*) Mean volume diameter, D_{mv} and (*d*) per cent of oil volume distribution in the third diameter peak, D_{p3}, for TC flow states ranging from LWV, TWV and TTV with a final concentration of 0.1% NSBM#4 oil mix, 100 ppm SERDP surfactant mix, 10 mM NaCl in distilled water at initial and final stages of mixing after injection. (Online version in colour.)

D_{p3}, similar to the no salt case. At the initial mixing stage (figure 7*a* at $t/\tau_v = 8.33$), the highest mean volume diameter, D_{mv}, was found for LWV ($Re = 700$) and TWV ($Re = 2040$ and 2700), to be around approx. 40 μm, and reduced on further increase in *Re* to approximately 30 μm for TTV ($Re = 4050$ and 5400), as shown in figure 7*a*. As before, the lower dispersion rates found at lower order flow states resulted in higher D_{mv}values, since more coalescence events can occur in the vortex where the emulsion was injected. The volume distribution as well as the values found were lower than the no salt case due to a decrease in interfacial tension with the presence of salt. However, the overall trend with mixing rate and flow state in the determination of DSD of emulsion stays similar in the initial mixing stage. The per cent volume distribution in the third peak diameter, D_{p3}, followed a similar trend, with the highest concentration found for LWV ($D_{p3} = 95$ μm at 38%) and observing a reduction with increase in *Re*. The lower D_{mv} (26 μm and 32 μm) and per cent volume distribution of D_{p3} ($D_{p3} = 115$ μm at approximately 16%) of TTV highlights the effects of intermixing rate as well as salt in forming relatively stable emulsions in the initial mixing stage.

For the final mixing stage, the highest mean volume diameter, D_{mv}, was observed for TWV, similar to the no salt case. However, for all turbulent cases, the mean volume diameter, D_{mv}increased for all *Re* values tested, with the highest values of around 50 μm found for TWV at $Re = 2040$ and TTV at $Re = 5400$. In the absence of salt, we observed coalescence was only dominant in the lower order flow states (LWV and TWV). We observed a combined effect of flocculation, aggregation and creaming leading to higher mean volume diameter but overall lower peak due to emulsion droplets potentially separating out. The salt effects make the analysis highly complicated; however, we found the emulsion to be less stable in the presence of salt as time progressed, even at higher flow states. At initial mixing stage with smaller timescale of observation and the reduced interfacial tension due to the addition of salt results in smaller diameter and a lower number of coalescence events. While this study provides an initial look at the salt effects, timescale and mixing rate effects, further detailed work is required to fully understand the stability of oily wastewater emulsions considering their highly complex nature.

(c) Dimensional analysis

The intermixing rate coefficients from the current study are of a similar order of magnitude with that by Wilkinson & Dutcher [42] using solid Kalliroscope tracer particles. However, certain differences between the two studies, such as the slight deviations from a power law type trend in the TWV regime, highlight that emulsion droplets are not necessarily perfect passive tracers of the flow. Other processes including separation, deformation, breakup and droplet-droplet dynamics influences mixing in flow. Using the typical droplet sizes determined in the prior section, the relative importance of these droplet processes can be determined through calculation of key dimensionless numbers in this section.

The emulsion oil droplets ($\rho_{\text{oil}} = 853\,\text{kg m}^{-3}$, droplet size ($D$) varying from 20 to 120 µm, determined in the prior section) were used in the current study to track the inter-vortex mass transfer instead of solid Kalliroscope tracers ($\rho_{\text{flakes}} = 1620\,\text{kg m}^{-3}$, particle size of $6 \times 30 \times 0.07\,\mu\text{m}^3$) [70], used in the previous work. A first step of looking at the differences in behaviour of the two systems, the settling velocity can be calculated using $v_t = g\ D^2\ (\rho_{\text{oil}} - \rho_{\text{medium}})/18\,\mu$. For the emulsion droplets, using the diameter of 50 µm and 100 µm, the settling velocity was found to be 2.02×10^{-4} and $8 \times 10^{-4}\,\text{m s}^{-1}$, and settling time of 42 min and 10.55 min, respectively, based on the annulus height. By comparison, the settling velocity of Kalliroscope flakes, assuming an effective diameter of approximately 1.44 µm, was $7.21 \times 10^{-7}\,\text{ms}^{-1}$ and settling time of the order of several hours (approx. 200 h). The passive tracers used previously can therefore stay suspended for a much longer duration compared with the larger emulsion droplets. By contrast, the largest emulsion droplets have the potential to separate out during the observed experiment time, which would conflate the measured intermixing coefficients.

The importance of the settling relative to the dispersion can be better determined by calculating a dispersive Péclet number, $Pe = Dv_t/D_z{}^*$, based on the settling timescales to the dispersion timescales. A 100 µm droplet diameter has a $Pe = 2.93 \times 10^{-3}$ at $Re = 700$ and 5.65×10^{-4} at $Re = 5400$. These values are all substantially less than unity, though especially at the lowest mixing speeds and largest droplet sizes (greater than 100 µm), a slight upward movement and separation of the droplets may occur, influencing both the measured intermixing rate and the DSD. By comparison, the solid tracer particles observed a much lower Pe number ranging from approximately 3.79×10^{-8} at $Re = 700$ to 7.32×10^{-9} at $Re = 5400$, indicating the creaming process to be much less significant for the small flakes than for the emulsified droplets.

Another difference between the larger droplets and the passive tracers is the ability of the droplets to deform in the flow. Using a conservative estimate of flow velocity experienced by the droplet based only on the global shear rate of the annulus, the capillary number, defined as $Ca = \text{v}_{\text{in}}\ \mu/\gamma$ (where v_{in} is the velocity of the inner cylinder, μ is the dynamic viscosity of the solution and γ is the interfacial tension, which was approximately $8\,\text{mN m}^{-1}$ as found previously for similar oil and surfactant concentration in [58,67]), Ca was found to be ranging from 1.00×10^{-2} at $Re = 700$ and 7.69×10^{-2} at $Re = 5400$. While less than unity, these values are still large enough to expect some small deformation due to the flow. In fact, the small deformations of droplets in response to an extensional flow field in a similar low capillary number regime are used for calculations of properties like interfacial tension [58]. As the droplet deforms in response to the local flow, its ability to act as a perfectly passive tracer similar to that of the solid Kalliroscope flakes is diminished. In addition, the presence of mixed flow kinematics also adds to the deformability of the droplet, as the regions of more extensional flow that occur in turbulent mixing and at the boundary between two vortices will lead to larger deformations than shear alone.

For emulsion dynamics in turbulent or higher Reynold number flows, a more relevant dimensionless quantity on droplet deformation, or even droplet breakup, is the Weber number, $We = \rho_{\mathrm{medium}}{}^{*}\mathrm{v_{in}}{}^{2}{}^{*}\mathrm{D}/\ \gamma$, which is the ratio of inertial forces to interfacial forces. A critical *We* defined in terms of turbulent fluctuations, such as the minimum eddy fluctuation velocity sufficient to breakup a droplet, has been used to determine droplet breakup in turbulent flows [71,72]. The *We* found here using the simpler expression above increased from 0.08 for $Re = 700$ to 4.94 for $Re = 5400$. In the turbulent regimes like TTV and TWV, the conditions found in this study indicate the droplet breakup is a plausible contributing explanation of the changes in DSD.

Finally, it should be noted that these systems are known to be unstable, with noticeable destabilization in jar tests of the order of tens of minutes to hours, depending on surfactant type and salt content [57,67,73]. Even during current experiments, the 4% NSBM#4 emulsion destabilized within 10–20 min, as observed with the change in the DSD even in the absence of flow. This destabilization required preparation of fresh sample before each experiment run. The salt can act to further destabilize the emulsion, by screening the charges on the ionic surfactants and decreasing the disjoining pressure in the film between the two droplets. Overall, the coalescence process is a balance of hydrodynamic, surface and disjoining forces [74,75].

Oily bilgewater emulsions are highly complex systems, which are different in a number of ways from passive tracers previously used. The relatively higher dispersive *Pe* indicates slight droplet upward movement and separation from solution, especially at lower *Re*, in contrast to the passive tracers, which can stay suspended for hours. The *Ca* and *We* indicate the potential for deformation of droplets, especially at higher order turbulent flows, indicating that in addition to the anticipated coalescence processes, changing the DSD in the TC flows can also be influenced by droplet breakup.

4. Conclusion

In this work, we have investigated the mixing dynamics of chemically stabilized oil-in-water emulsions in a well-controlled hydrodynamic environment established by our TC cell with radial fluid injection. The apparent intermixing rates of concentrated emulsions for three different flow states including LWV, TWV and TTV at five different Reynolds numbers were determined in both distilled water and saline environment. In addition, the DSD of the emulsion was measured at two different stages of mixing to observe the intermixing rate, observation timescale and salinity effect on the emulsion stability.

The apparent intermixing coefficient, *k*, was generally found to be increasing with increasing *Re*. This increase is similar to previous studies by Nemri *et al*. and Wilkinson & Dutcher [33,42]. However, there were certain slight differences in the rate of increase between these studies since emulsion droplets were used here for tracking the intermixing coefficient instead of solid tracer particles, which were used previously. Emulsion droplets can affect the mixing in the TC cell due to their settling time, ability to coalesce, aggregate and deform/breakup in the flow, and relative position in the vortex flow. Hence the apparent intermixing coefficients calculated here are likely influenced by these characteristics.

In addition to the apparent intermixing coefficients, the DSDs of the emulsions were measured at different stages of mixing to determine the effects of observation timescale on destabilization as emulsions are inherently unstable and tend to destabilize over time. The time of observation was divided into initial mixing stage (10 min) and the final mixing stage (30 min). From the DSD analysis, it was found that for both initial and final mixing stages, the intermixing and DSD were closely related. Mixing in the TC flow leads to a variety of effects, including shear-induced coalescence, flocculation, aggregation, breakup and creaming in emulsion as previously discovered for simple shear flow [50–55]. In fact, the presence of radial inflow may also cause enhanced mixing dynamics over traditional TC flow [76,77]. The relatively lower mixing rates of LWV and lower end TWV flow states resulted in more shear-induced coalescence and higher mean volume diameter, D_{mv}, and higher oil volume fraction of third diameter peak, D_{p3}. The higher intermixing rates of TTV flow state resulted in smaller droplets with more uniformly distributed emulsion with lower D_{mv}. The effects of the emulsions destabilizing over time can be seen in the final mixing stage. The highest D_{mv} observed was 58 µm for TWV at $Re = 2040$, which was lower than the initial mixing stage, potentially due to the emulsion destabilizing over time by creaming and larger oil droplets separating out of the solution, accounting for the reduced droplet size. Overall, the lower Re range of TWV was found to be optimal for forming unstable emulsion both at initial mixing stages due to lower dispersion rates, and at the final mixing stage due to optimal shear rates to drive maximum droplet coalescence. These types of emulsion formed during mixing at TWV would be easier to treat during a liquid–liquid phase separation process, as more oil volume fraction is concentrated in larger sized droplets.

Lastly, the impact of a saline environment in combination with the observation timescale and mixing rates on the emulsion droplet size changes provides a preliminary look at the effects of salt on emulsion stability in TC flow. Initially overall, the D_{mv} and D_{p3} oil volume fraction values found for the salt case were lower compared with the no salt case. Whereas in the final stages of mixing, the salt resulted in higher droplet sizes and more unstable emulsion. In the presence of salt, the apparent intermixing coefficients, k, were also found to be higher than the no salt case, presumably due to the changes in the droplet size and stability. Ultimately, the work performed in this study can be helpful in creating unstable emulsions for easier separation and treatment by controlling the formation conditions and mixing dynamics.

Data accessibility. Supporting data can be found at: https://doi.org/10.13020/snhb-yp37 [78]. The mass transfer results for the 10 mM NaCl systems are provided in the electronic supplementary material [79].

Authors' contributions. V.P.: conceptualization, data curation, formal analysis, investigation, methodology, software, visualization, writing—original draft and writing—review and editing; C.V.: investigation; C.D.: conceptualization, supervision and writing—review and editing.

All authors gave final approval for publication and agreed to be held accountable for the work performed therein.

Conflict of interest declaration. We declare we have no competing interests.

Funding. This material is based upon work supported by the Humphreys Engineer Center Support Activity under initial contract No. W912HQ18C0024 and follow-on contract No. W912HQ20C0041, corresponding to the DOD Strategic Environmental Research and Development Program (SERDP) initial project WP18-1031 and follow-on project WP19-1407, respectively. Portions of this work were conducted in the Minnesota Nano Center, which is supported by the National Science Foundation through the National Nanotechnology Coordinated Infrastructure (NNCI) under Award Number ECCS-2025124. In addition, C.V. contributed to the work during a summer research experience at the University of Minnesota, supported by the Research Experiences for Undergraduates (REU) Program of the National Science Foundation under Award Number DMR-1852044 and through the University of Minnesota MRSEC under Award Number DMR-2011401.

Acknowledgement. We would like to thank Dr. Jared Church at Naval Surface Warfare Center Carderock Division (NSWCCD) for many helpful conversations.

References

1. Taylor GI. 2006 VIII. Stability of a viscous liquid contained between two rotating cylinders. *Phil. Trans. R. Soc. Lond. Ser. A Contain Pap. Math. Phys. Character.* **223**, 289–343.
2. Coles D. 1965 Transition in circular Couette flow. *J. Fluid Mech.* **21**, 385–425. (doi:10.1017/S0022112065000241)
3. Snyder HA. 1970 Waveforms in rotating Couette flow. *Int. J. Non Linear Mech.* **5**, 659–685. (doi:10.1016/0020-7462(70)90055-7)
4. Jones CA. 1985 The transition to wavy Taylor vortices. *J. Fluid Mech.* **157**, 135–162. (doi:10.1017/S0022112085002336)

5. Walsh TJ, Donnelly RJ. 1988 Taylor-Couette flow with periodically corotated and counterrotated cylinders. *Phys. Rev. Lett.* **60**, 700–703. (doi:10.1103/PhysRevLett.60.700)
6. Andereck CD, Dickman R, Swinney HL. 1983 New flows in a circular Couette system with co-rotating cylinders. *Phys. Fluids* **26**, 1395–1401. (doi:10.1063/1.864328)
7. Andereck CD, Liu SS, Swinney HL. 1986 Flow regimes in a circular Couette system. *J. Fluid Mech.* **164**, 155–183. (doi:10.1017/S0022112086002513)
8. Dutcher CS, Muller SJ. 2007 Explicit analytic formulas for Newtonian Taylor-Couette primary instabilities. *Phys. Rev. E* **75**, 047301. (doi:10.1103/PhysRevE.75.047301)
9. Dutcher CS, Muller SJ. 2009 Spatio-temporal mode dynamics and higher order transitions in high aspect ratio Newtonian TaylorCouette flows. *J. Fluid Mech.* **641**, 85–113. (doi:10.1017/S0022112009991431)
10. Cagney N, Balabani S. 2019 Taylor-Couette flow of shear-thinning fluids. *Phys. Fluids* **31**, 053102. (doi:10.1063/1.5088143)
11. Ashrafi N. 2011 Stability analysis of shear-thinning flow between rotating cylinders. *Appl. Math. Model* **35**, 4407–4423. (doi:10.1016/j.apm.2011.03.010)
12. Dutcher CS, Muller SJ. 2013 Effects of moderate elasticity on the stability of co- and counter-rotating Taylor–Couette flows. *J. Rheol. (N Y N Y).* **57**, 791–812. (doi:10.1122/1.4798549)
13. Baumert BM, Muller SJ. 1999 Axisymmetric and non-axisymmetric elastic and inertio-elastic instabilities in Taylor-Couette flow. *J. Nonnewton Fluid Mech.* **83**, 33–69. (doi:10.1016/S0377-0257(98)00132-3)
14. Larson RG, Muller SJ, Shaqfeh ESG. 1994 The effect of fluid rheology on the elastic Taylor-Couette instability. *J. Nonnewton Fluid Mech.* **51**, 195–225. (doi:10.1016/0377-0257(94)85012-7)
15. Thomas DG, Khomami B, Sureshkumar R. 2009 Nonlinear dynamics of viscoelastic Taylor-Couette flow: effect of elasticity on pattern selection, molecular conformation and drag. *J. Fluid Mech.* **620**, 353–382. (doi:10.1017/S0022112008004710)
16. Panwar V, Metaxas AE, Dutcher CS. 2021 Polyelectrolyte solutions in Taylor-Couette flows. *J. Nonnewton Fluid Mech.* **295**, 104617. (doi:10.1016/j.jnnfm.2021.104617)
17. Coufort C, Bouyer D, Liné A. 2005 Flocculation related to local hydrodynamics in a Taylor–Couette reactor and in a jar. *Chem. Eng. Sci.* **60**, 2179–2192. (doi:10.1016/j.ces.2004.10.038)
18. Ameer GA, Barabino G, Sasisekharan R, Harmon W, Cooney CL, Langer R. 1999 Ex vivo evaluation of a Taylor-Couette flow, immobilized heparinase I device for clinical application. *Proc. Natl Acad. Sci. USA* **96**, 2350–2355. (doi:10.1073/pnas.96.5.2350)
19. Metaxas AE, Panwar V, Olson RL, Dutcher CS. 2021 Ionic strength and polyelectrolyte molecular weight effects on floc formation and growth in Taylor–Couette flows. *Soft Matter.* **17**, 1246–1257. (doi:10.1039/D0SM01517B)
20. Schrimpf M, Esteban J, Warmeling H, Färber T, Behr A, Vorholt AJ. 2021 Taylor-Couette reactor: principles, design, and applications. *AIChE J.* **67**, e17228. (doi:10.1002/aic.17228)
21. Crumeyrolle O, Mutabazi I, Grisel M. 2002 Experimental study of inertioelastic Couette-Taylor instability modes in dilute and semidilute polymer solutions. *Phys. Fluids* **14**, 1681–1688. (doi:10.1063/1.1466837)
22. Denn MM, Roisman JJ. 1969 Rotational stability and measurement of normal stress functions in dilute polymer solutions. *AIChE J.* **15**, 454–459. (doi:10.1002/aic.690150328)
23. Hammond TG, Hammond JM. 2001 Optimized suspension culture: the rotating-wall vessel. *Am. J. Physiol. Ren. Physiol.* **281**, 12–25. (doi:10.1152/ajprenal.2001.281.1.F12)
24. Spaulding GF, Jessup JM, Goodwin TJ. 1993 Advances in cellular construction. *J. Cell. Biochem.* **51**, 249–251. (doi:10.1002/jcb.240510302)
25. Tsao YMD, Boyd E, Wolf DA, Spaulding G. 2012 Fluid dynamics within a rotating bioreactor in space and Earth environments. *J. Spacecraft. Rockets* **31**, 937–943. (doi:10.2514/3.26541)
26. Kim M *et al.* 2014 Preparation of black pigment with the Couette-Taylor vortex for electrophoretic displays. *Chem. Eng. Sci.* **119**, 245–250. (doi:10.1016/j.ces.2014.08.036)
27. Kong B, Vigil RD. 2013 Light-limited continuous culture of Chlorella vulgaris in a Taylor vortex reactor. *Environ. Prog. Sustain. Energy* **32**, 884–890. (doi:10.1002/ep.11834)
28. Krintiras GA, Gadea Diaz J, Van Der Goot AJ, Stankiewicz AI, Stefanidis GD. 2016 On the use of the Couette Cell technology for large scale production of textured soy-based meat replacers. *J. Food Eng.* **169**, 205–213. (doi:10.1016/j.jfoodeng.2015.08.021)
29. Sczechowski JG, Koval CA, Noble RD. 1995 A Taylor vortex reactor for heterogeneous photocatalysis. *Chem. Eng. Sci.* **50**, 3163–3173. (doi:10.1016/0009-2509(95)00176-6)

30. Haut B, Ben Amor H, Coulon L, Jacquet A, Halloin V. 2003 Hydrodynamics and mass transfer in a Couette–Taylor bioreactor for the culture of animal cells. *Chem. Eng. Sci.* **58**, 777–784. (doi:10.1016/S0009-2509(02)00607-3)
31. Metaxas A, Wilkinson N, Raethke E, Dutcher CS. 2018 In situ polymer flocculation and growth in Taylor-Couette flows. *Soft Matter.* **14**, 8627–8635. (doi:10.1039/C8SM01694A)
32. Liu L *et al.* 2022 Effect of hydrodynamic heterogeneity on particle dispersion in a Taylor-Couette flow reactor with variable configurations of inner cylinder. *J. Taiwan Inst. Chem. Eng.* **131**, 104141. (doi:10.1016/j.jtice.2021.11.008)
33. Nemri M, Charton S, Climent E. 2016 Mixing and axial dispersion in Taylor–Couette flows: the effect of the flow regime. *Chem. Eng. Sci.* **139**, 109–124. (doi:10.1016/j.ces.2015.09.022)
34. Ohmura N, Kataoka K, Shibata Y, Makino T. 1997 Effective mass diffusion over cell boundaries in a Taylor-Couette flow system. *Chem. Eng. Sci.* **52**, 1757–1765. (doi:10.1016/S0009-2509(97)00012-2)
35. Ohmura N, Makino T, Motomura A, Shibata Y, Kataoka K. 1998 Intercellular mass transfer in wavy/turbulent Taylor vortex flow. *Int. J. Heat Fluid Flow* **19**, 159–166. (doi:10.1016/S0142-727X(97)10020-0)
36. Dusting J, Balabani S. 2009 Mixing in a Taylor–Couette reactor in the non-wavy flow regime. *Chem. Eng. Sci.* **64**, 3103–3111. (doi:10.1016/j.ces.2009.03.046)
37. Nemri M, Cazin S, Charton S, Climent E. 2014 Experimental investigation of mixing and axial dispersion in Taylor–Couette flow patterns. *Exp. Fluids* **55**, 1–16. (doi:10.1007/s00348-014-1769-6)
38. Campero RJ, Vigil RD. 1997 Axial dispersion during low Reynolds number Taylor-Couette flow: intra-vortex mixing effects. *Chem. Eng. Sci.* **52**, 3303–3310. (doi:10.1016/S0009-2509(97)00151-6)
39. Desmet G, Verelst H, Baron GV. 1996 Local and global dispersion effects in Couette-Taylor flow—I. Description and modeling of the dispersion effects. *Chem. Eng. Sci.* **51**, 1287–1298. (doi:10.1016/0009-2509(95)00381-9)
40. Desmet G, Verelst H, Baron GV. 1996 Local and global dispersion effects in Couette-Taylor flow—II. Quantitative measurements and discussion of the reactor performance. *Chem. Eng. Sci.* **51**, 1299–1309. (doi:10.1016/0009-2509(95)00382-7)
41. Wilkinson N, Dutcher CS. 2017 Taylor-Couette flow with radial fluid injection. *Rev. Sci. Instrum.* **88**, 083904. (doi:10.1063/1.4997340)
42. Wilkinson NA, Dutcher CS. 2018 Axial mixing and vortex stability to in situ radial injection in Taylor-Couette laminar and turbulent flows. *J. Fluid Mech.* **854**, 324–347. (doi:10.1017/jfm.2018.596)
43. McLaughlin C, Falatko D, Danesi R, Albert R. 2014 Characterizing shipboard bilgewater effluent before and after treatment. *Environ. Sci. Pollut. Res.* **21**, 5637–5652. (doi:10.1007/s11356-013-2443-x)
44. Asselin M, Drogui P, Brar SK, Benmoussa H, Blais JF. 2008 Organics removal in oily bilgewater by electrocoagulation process. *J. Hazard. Mater.* **151**, 446–455. (doi:10.1016/j.jhazmat.2007.06.008)
45. Tomaszewska M, Orecki A, Karakulski K. 2005 Treatment of bilge water using a combination of ultrafiltration and reverse osmosis. *Desalination* **185**, 203–212. (doi:10.1016/j.desal.2005.03.078)
46. Copeland C. 2008 Cruise ship pollution: Background, laws and regulations, and key issues.
47. Kajitvichyanukul P, Hung YT, Wang LK. 2006 Oil water separation. *Adv. Physicochem. Treat Process* **4**, 521–548. (doi:10.1007/978-1-59745-029-4_16)
48. Church J *et al.* 2019 Identification and characterization of bilgewater emulsions. *Sci. Total Environ.* **691**, 981–995. (doi:10.1016/j.scitotenv.2019.06.510)
49. Farzad R, Puttinger S, Pirker S, Schneiderbauer S. 2018 Investigation of droplet size distribution for liquid-liquid emulsions in Taylor-Couette flows. *J. Dispers. Sci. Technol.* **39**, 250–258. (doi:10.1080/01932691.2017.1312431)
50. Nandi A, Khakhar DV, Mehra A. 2001 Coalescence in surfactant-stabilized emulsions subjected to shear flow. *Langmuir* **17**(9), 2647–2655. (https://doi.org/10.1021/la001473m)
51. Nandi A, Mehra A, Khakhar DV. 2006 Coalescence in a surfactant-less emulsion under simple shear flow. *AIChE J.* **52**, 885–894. (doi:10.1002/aic.10682)

52. Thivilliers-Arvis F, Laurichesse E, Eronique Schmitt V, Leal-Calderon F. 2010 Shear-induced instabilities in oil-in-water emulsions comprising partially crystallized droplets. *Langmuir* **26**, 16782–16790. (doi:10.1021/la1027288)
53. van Boekel MAJS, Walstra P. 1981 Effect of Couette flow on stability of oil-in-water emulsions. *Colloids Surf.* **3**, 99–107. (doi:10.1016/0166-6622(81)80070-4)
54. Whitby CP, Fischer FE, Fornasiero D, Ralston J. 2011 Shear-induced coalescence of oil-in-water Pickering emulsions. *J. Colloid Interface Sci.* **361**, 170–177. (doi:10.1016/j.jcis.2011.05.046)
55. Yeung A, Moran K, Masliyah J, Czarnecki J. 2003 Shear-induced coalescence of emulsified oil drops. *J. Colloid Interface Sci.* **265**, 439–443. (doi:10.1016/S0021-9797(03)00531-9)
56. Czarnecki J. 1985 The effects of surface inhomogeneities on the interactions in colloidal systems and colloid stability. *Adv. Colloid Interface Sci.* **24**, 283–319. (doi:10.1016/0001-8686(85)80035-X)
57. Diaz D *et al.* 2021 Evaluation of bilgewater emulsion stability using nondestructive analytical methods. *Ind. Eng. Chem. Res.* **60**, 1014–1025. (doi:10.1021/acs.iecr.0c04814)
58. Chen Y, Dutcher CS. 2020 Size dependent droplet interfacial tension and surfactant transport in liquid-liquid systems, with applications in shipboard oily bilgewater emulsions. *Soft Matter.* **16**, 2994–3004. (doi:10.1039/C9SM01892A)
59. Czarny O, Lueptow RM. 2007 Time scales for transition in Taylor-Couette flow. *Phys. Fluids* **19**, 54103. (doi:10.1063/1.2728785)
60. Snyder HA. 1969 Wave-number selection at finite amplitude in rotating Couette flow. *J. Fluid Mech.* **35**, 273–298. (doi:10.1017/S002211206900111X)
61. Park K, Crawford GL, Donnelly RJ. 1981 Determination of transition in Couette flow in finite geometries. *Phys. Rev. Lett.* **47**, 1448. (doi:10.1103/PhysRevLett.47.1448)
62. Koga JK, Koschmieder EL. 1998 Taylor vortices in short fluid columns. *Phys. Fluids A Fluid Dyn.* **1**, 1475. (doi:10.1063/1.857325)
63. Park K, Crawford GL, Donnelly RJ. 1983 Characteristic lengths in the wavy vortex state of Taylor-Couette flow. *Phys. Rev. Lett.* **51**, 1352. (doi:10.1103/PhysRevLett.51.1352)
64. King GP, Swinney HL. 1983 Limits of stability and irregular flow patterns in wavy vortex flow. *Phys. Rev. A* **27**, 1240. (doi:10.1103/PhysRevA.27.1240)
65. Wereley ST, Lueptow RM. 1994 Azimuthal velocity in supercritical circular Couette flow. *Exp. Fluids* **18**, 1–9. (doi:10.1007/BF00209355)
66. Neitzel GP. 1984 Numerical computation of time-dependent Taylor-vortex flows in finite-length geometries. *J. Fluid Mech.* **141**, 51–66. (doi:10.1017/S0022112084000732)
67. Church J, Paynter DM, Lee WH. 2017 In situ characterization of oil-in-water emulsions stabilized by surfactant and salt using microsensors. *Langmuir* **33**, 9731–9739. (doi:10.1021/acs.langmuir.7b01558)
68. Krebs T, Schroën K, Boom R. 2012 Coalescence dynamics of surfactant -stabilized emulsions studied with microfluidics. *Soft Matter.* **8**, 10 650–10 657. (doi:10.1039/c2sm26122g)
69. Davis CR, Martinez CJ, Howarter JA, Erk KA. 2021 Impact of saltwater environments on the coalescence of oil-in-water emulsions stabilized by an anionic surfactant. *ACS ES&T Water* **1**, 1702–1713. (doi:10.1021/acsestwater.1c00066)
70. Borrero-Echeverry D, Crowley CJ, Riddick TP. 2018 Rheoscopic fluids in a post-Kalliroscope world. *Phys Fluids* **30**, 087103. (https://doi.org/10.1063/1.5045053)
71. Eskin D, Taylor SD, Yang D. 2017 Modeling of droplet dispersion in a turbulent Taylor–Couette flow. *Chem. Eng. Sci.* **161**, 36–47. (doi:10.1016/j.ces.2016.12.008)
72. Hesketh RP, Fraser Russell TW, Etchells AW. 1987 Bubble size in horizontal pipelines. *AIChE J.* **33**, 663–667. (doi:10.1002/aic.690330414)
73. Church J, Daniels GC, Lundin JG, Lee WH, Paynter D. 2021 Stabilization of bilgewater emulsions by shipboard oils. *ACS ES&T Water* **1**, 1745–1755. (doi:10.1021/acsestwater.1c00102)
74. Chatzigiannakis E, Jaensson N, Vermant J. 2021 Thin liquid films: where hydrodynamics, capillarity, surface stresses and intermolecular forces meet. *Curr. Opin. Colloid Interface Sci.* **53**, 101441. (doi:10.1016/j.cocis.2021.101441)
75. Narayan S, Metaxas AE, Bachnak R, Neumiller T, Dutcher CS. 2020 Zooming in on the role of surfactants in droplet coalescence at the macroscale and microscale. *Curr. Opin. Colloid Interface Sci.* **50**, 101385. (doi:10.1016/j.cocis.2020.08.010)

76. Ilin K, Morgulis A. 2013 Instability of an inviscid flow between porous cylinders with radial flow. *J. Fluid Mech.* **730**, 364–378. (doi:10.1017/jfm.2013.357)
77. Kerswell RR. 2015 Instability driven by boundary inflow across shear: a way to circumvent Rayleigh's stability criterion in accretion disks? *J. Fluid Mech.* **784**, 619–663. (doi:10.1017/jfm.2015.613)
78. Panwar V, Vargas CN, Dutcher CS. 2023 Supporting data for 'Dispersion and mixing dynamics of complex oil-inwater emulsions in Taylor–Couette flows'. Digital Repository. (doi:10.13020/snhb-yp37)
79. Panwar V, Vargas CN, Dutcher CS. 2023 Dispersion and mixing dynamics of complex oil-in-water emulsions in Taylor–Couette flows. Figshare. (doi:10.6084/m9.figshare.c.6430088.v3)